Eur. Phys. J. C 8, 393–401 (1999)
DOI 10.1007/s100529901082

THE EUROPEAN PHYSICAL JOURNAL C

Measurement of helicity parameters in top quark decay

Ch.A. Nelson[a], A.M. Cohen

Department of Physics, State University of New York at Binghamton, Binghamton, NY 13902-6016, USA

Received: 12 November 1998 / Published online: 27 April 1999

Abstract. It is important to be able to quantitatively assay future measurements of competing observables consistent with the g_{V-A} coupling predictions for $t \to W^+ b$ decay, so plots of the values of these helicity parameters are given in terms of a " $(V-A)$ + Additional Lorentz Structure". Three phase-type ambiguities are shown to exist, but measurement of the sign of the large interference between the W longitudinal/transverse amplitudes will resolve two of them. The large m_b effects in both b_L and b_R amplitudes from some couplings demonstrate that it is less model dependent to measure helicity parameters, instead of setting limits on some arbitrary subset of coupling constants.

1 Motivations

Initial tests of the Lorentz structure of $t \to W^+ b$ decay can be carried out at the Tevatron[1], but the more precise measurements will be possible at the CERN LHC [2] and at a NLC [3]. It is important to be able to quantitatively assay future measurements of competing observables consistent with the standard model (SM) prediction of only a g_{V-A} coupling. For this purpose, plots are given below of the values of the helicity parameters in terms of a "$(V-A)$ + Additional Lorentz Structure" versus effective-mass scales for new physics, Λ_i, associated with specific additional Lorentz structures. In effective field theory, Λ_i, is the scale [4] at which new particle thresholds or new dynamics are expected to occur; Λ_i can also be interpreted as a measure of a top quark compositeness scale.

Three phase-type ambiguities versus the SM prediction are shown to exist: two with low effective mass scales, $g_{V-A} + g_{S+P}$ with $\Lambda_{S+P} \sim -35 GeV$ and $g_{V-A} + g_{f_M + f_E}$ with $\Lambda_{f_M+f_E} \sim 53 GeV$, and a third due to an arbitrary sign-flip in the b_L-amplitudes $A_X(\lambda_b = -1/2) = -A_{V-A}$ $(\lambda_b = -1/2)$. The first two of these ambiguities can be resolved by measurement of the sign of the large interference between the W longitudinal/transverse amplitudes. Measurement of the sign of the η_L helicity parameter will determine the sign of $cos\beta_L$ where β_L is the relative phase of the two b_L-amplitudes ($\eta_L = \pm 0.46$ where the upper sign is for the SM). Both from the perspective of carefully testing the SM and that of searching for new physics, we believe that it is very important that experiments measure this W longitudinal/transverse interference parameter (the LHC should be sensitive to ~ 3 % and the Tevatron in a Run 3 to perhaps the ~ 10 % level). Simultaneously, such experiments should bound, or measure, the $\tilde{T}_{FS}$ violating ${\eta_L}'$ parameter which can be sizable for low-effective mass scales: ${\eta_L}' \sim \pm 0.3$ for a pure imaginary additional coupling Λ_{S+P} or $\Lambda_{f_M+f_E} \sim \pm i 50 GeV$.

Since the helicity parameters appear directly in the various polarization and spin-correlation functions, it is clearly more model independent to simply measure them rather than to set limits on an " ad hoc" set of additional coupling constants. The large m_b effects in both b_L and b_R amplitudes explicitly demonstrate this point. In many cases, finite m_b effects lead to sizable " oval shapes" as the effective mass scale Λ_i varies, see Figs. 2, 4, 8, 9.

Resolution of the third ambiguity, as well as determination of two remaining independent relative phases (e.g. α_0 and γ_+) necessary for a complete amplitude measurement of $t \to W^+ b$ decay, will require direct empirical information about the b_R-amplitudes. One way would be from a Λ_b polarimetry measurement [5] of the b-polarimetry interference parameters ϵ_+ and κ_0. Even at an NLC, such measurements will be difficult unless certain non-SM couplings occur. In particular, here additional $S+P$ and $f_M + f_E$ couplings have negligible effects, but non-chiral couplings like V or A, f_M or f_E (for ϵ_+), S or P (for κ_0) can produce large effects, see below.

2 Helicity amplitudes and α, β, γ relative phases

For $t \to W^+ b$ decay, the four on-shell helicity amplitudes $A(\lambda_{W^+}, \lambda_b)$ can be uniquely determined by measurement of four moduli and three relative phases. In Fig. 1, measurements in the right and left columns are respectively of order $\mathcal{O}(L^2)$ and $\mathcal{O}(R^2)$. The interference measurements between the two columns are of order $\mathcal{O}(LR)$. L and R denote the b quark's helicity $\lambda_b = \mp 1/2$. Numerical values of $A(\lambda_{W^+}, \lambda_b)$ for the standard model(SM) are given in the top row of Table 1. For the pure $V-A$ coupling of the standard model, the left-handed helicity $\lambda_b = -1/2$

[a] e-mail: cnelson@bingvmb.cc.binghamton.edu

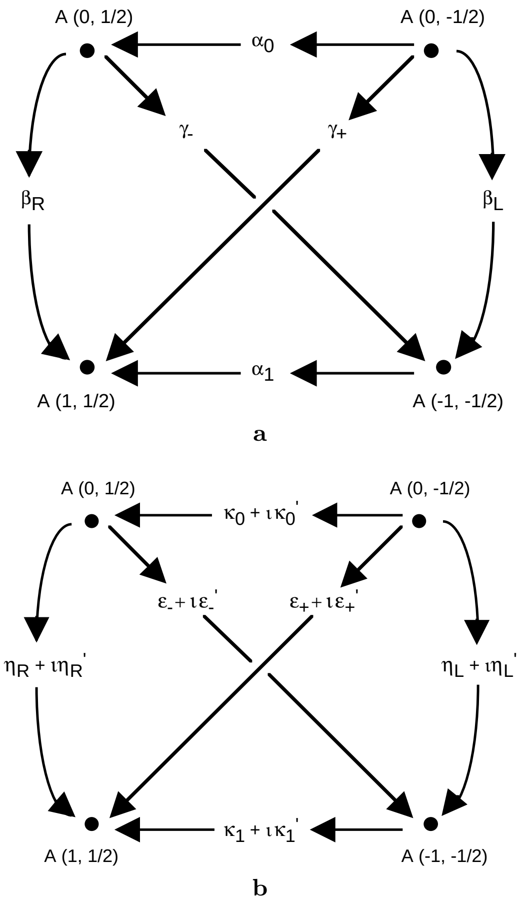

Fig. 1a,b. For $t \to W^+ b$ decay, display of the four helicity amplitudes $A(\lambda_{W^+}, \lambda_b)$ relative to the b quark's helicity. The **upper sketch** defines the measurable "α, β, γ" relative phases, c.f. (1). The **lower sketch** defines the real part and imaginary part (primed) helicity parameters corresponding to these relative phases. Measurement of the sign of η_L determines the relative phase of the $\lambda_b = -1/2$ amplitudes and would resolve the first two ambiguities (compare Tables 1 and 2)

amplitudes dominate by 1 to 2 orders of magnitude for $m_b \sim 4.5GeV$. Intrinsic and relative signs of these helicity amplitudes are determined by the Jacob-Wick phase convention. The layout of the corners in Fig. 1 has been chosen to reflect the layout in the following probability plots for $P(W_L)$ versus $P(b_L)$ where

$$P(W_L) = \text{Probability } W^+ \text{ is longitudinally polarized, } \lambda_{W^+} = 0$$
$$P(b_L) = \text{Probability } b \text{ is left-handed, } \lambda_b = -1/2$$

The "arrows" in the upper part of Fig. 1 define the measurable α, β, γ relative phases between the four amplitudes. For instance,

$$\alpha_0 = \phi_0^R - \phi_0^L, \ \beta_L = \phi_{-1}^L - \phi_0^L, \ \gamma_+ = \phi_1^R - \phi_0^L \tag{1}$$

where $A(\lambda_{W^+}, \lambda_b) = |A| \exp(i\phi^{L,R}_{\lambda_{W^+}})$. So for a pure $V - A$ coupling, the β's vanish and all the α's and γ's equal $+\pi$ (or $-\pi$) to give the intrinsic minus sign of the standard model's b_R amplitudes, see top row of Table 1.

Table 1. For the ambiguous moduli points, numerical values of the associated helicity amplitudes $A(\lambda_{W^+}, \lambda_b)$. The values for the amplitudes are listed first in $g_L = 1$ units, and second as $A_{new} = A_{g_L=1}/\sqrt{\Gamma}$ which removes the effect of the differing partial width, Γ for $t \to W^+ b$. [$m_t = 175GeV$, $m_W = 80.35GeV$, $m_b = 4.5GeV$]

	$A(0, -\frac{1}{2})$	$A(-1, -\frac{1}{2})$	$A(0, \frac{1}{2})$	$A(1, \frac{1}{2})$
$A_{g_L=1}$ in $g_L = 1$ units				
$V - A$	338	220	-2.33	-7.16
$S + P$	-338	220	-24.4	-7.16
$f_M + f_E$	220	-143	1.52	-4.67
$A_{New} = A_{g_L=1}/\sqrt{\Gamma}$				
$V - A$	0.84	0.54	-0.0058	-0.018
$S + P$	-0.84	0.54	-0.060	-0.018
$f_M + f_E$	0.84	-0.54	0.0058	-0.018

The lower part of Fig. 1 displays the real part and imaginary part (primed) helicity parameters corresponding to interference measurements of the respective relative phases. For instance, c.f. Appendix B,

$$\begin{aligned} \eta_L &\equiv \tfrac{1}{\Gamma}|A(-1, -\tfrac{1}{2})||A(0, -\tfrac{1}{2})| \cos \beta_L \\ \eta_L' &\equiv \tfrac{1}{\Gamma}|A(-1, -\tfrac{1}{2})||A(0, -\tfrac{1}{2})| \sin \beta_L \end{aligned} \tag{2}$$

and

$$\eta_{L,R} = \frac{1}{2}(\eta \pm \omega) \tag{3}$$

In the absence of $\tilde{T}_{FS}$ violation, the relative phases will be interger multiples of π and all prime parameters will vanish.

By Λ_b polarimetry[5], or some other b-polarimetry technique, it would be possible to measure the α and γ relative phase. In the standard model, the two helicity parameters between the amplitudes with the largest moduli are

$$\begin{aligned} \kappa_0 &\equiv \tfrac{1}{\Gamma}|A(0, \tfrac{1}{2})||A(0, -\tfrac{1}{2})| \cos \alpha_0 \\ \epsilon_+ &\equiv \tfrac{1}{\Gamma}|A(1, \tfrac{1}{2})||A(0, -\tfrac{1}{2})| \cos \gamma_+ \end{aligned} \tag{4}$$

We refer to κ_0, ϵ_+ as the "b-polarimetry interference parameters". From Figs. 1 other combinations of relative-phases/helicity-parameters are mathematically equivalent. Unfortunately from the perspective of a complete measurement of the four helicity amplitudes, the tree-level values of κ_0, ϵ_+ in the SM are only about 1%. See the top line in both parts of Table 2, which lists the $V - A$ values of the helicity parameters for $m_b = 4.5GeV$.

In the plots below, the values of the helicity parameters are given in terms of a "$(V - A)$ + Additional Lorentz Structure". Generically, we denote these additional couplings by

$$g_{Total} \equiv g_L + g_X \tag{5}$$

$$X = \begin{cases} X_c = \text{ chiral} = \{V + A, S \pm P, f_M \pm f_E\} \\ X_{nc} = \text{ non-chiral} = \{V, A, S, P, f_M, f_E\}. \end{cases}$$

Table 2. For the ambiguous moduli points, numerical values of the associated helicity parameters. Listed first are the four moduli parameters. Listed second are the values of the interference parameters which could be used to resolve the ambiguities

	σ	ξ	ζ	$\Gamma[GeV]$	
$V-A$	0.41	1.00	0.41	$1.55GeV$	
$S+P$	0.41	0.99	0.40	$1.55GeV$	
f_M+f_E	0.41	1.00	0.41	$0.66GeV$	
	η	ω	η_L	κ_o	ϵ_+
$V-A$	0.46	0.46	0.46	-0.005	-0.015
$S+P$	-0.45	-0.46	-0.46	-0.05	0.015
f_M+f_E	-0.46	-0.46	-0.46	0.005	-0.015

For $t \to W^+ b$, the most general Lorentz coupling is $W_\mu^* J_{bt}^\mu = W_\mu^* \bar{u}_b(p) \Gamma^\mu u_t(k)$ where $k_t = q_W + p_b$, and

$$\Gamma_V^\mu = g_V \gamma^\mu + \frac{f_M}{2\Lambda}\iota\sigma^{\mu\nu}(k-p)_\nu + \frac{g_{S^-}}{2\Lambda}(k-p)^\mu + \frac{g_S}{2\Lambda}(k+p)^\mu + \frac{g_{T^+}}{2\Lambda}\iota\sigma^{\mu\nu}(k+p)_\nu \qquad (6)$$

$$\Gamma_A^\mu = g_A \gamma^\mu\gamma_5 + \frac{f_E}{2\Lambda}\iota\sigma^{\mu\nu}(k-p)_\nu\gamma_5 + \frac{g_{P^-}}{2\Lambda}(k-p)^\mu\gamma_5 + \frac{g_P}{2\Lambda}(k+p)^\mu\gamma_5 + \frac{g_{T_5^+}}{2\Lambda}\iota\sigma^{\mu\nu}(k+p)_\nu\gamma_5 \qquad (7)$$

For $g_L = 1$ units with $g_i = 1$, the nominal size of Λ_i is $\frac{m_t}{2} = 88GeV$, see below.

Lorentz equivalence theorems for these couplings are treated in Appendix A. Explicit expressions for the $A(\lambda_{W^+}, \lambda_b)$ in the case of these additional Lorentz structures are given in [5]. Other recent general analyses of effects in $t \to W^+ b$ decay associated with new physics arising from large effective- mass scales Λ_i are in [6-12]. Some work on higher order QCD and EW corrections has been done in [13]. It is much less model dependent to determine the helicity parameters directly from experimental data instead of assuming an arbitrary set of couplings and an ad hoc m_b treatment to determine limits on g_i's. *There do not exist* "Lorentz equivalence theorems" with-respect-to both m_b dependence and a minimal set of couplings *when* m_b is allowed to vary. The theorems of appendix A are *only* for a fixed m_b value.

In Fig. 2 are two probability plots for $P(W_L) = \frac{1+\sigma}{2}$ versus $P(b_L) = \frac{1+\xi}{2}$. The upper plot is for the case of a single additional chiral coupling g_i. The corners correspond to those of Fig. 1. So the dark rectangle of the SM, gives the relative magnitude of the square of the moduli of its four basic helicity amplitudes. Also, note from the dashed horizontal oval that an additional $V + A$ coupling does not change the SM expectation that approximately 70% of the final W's in $t \to W^+ b$ decay will be longitudinally polarized.

The endpoints of each oval are at the dark SM rectangle and the dark ellipse where the coupling is pure g_i. In general, the non-zero area of an oval depends monotonically on $m_b = 4.5GeV$ and the area will increase if a larger value is chosen for m_b. The captions to the figures in this paper discuss the signs of effective-mass scales Λ_i associated with the two parts of each oval which lie between the two endpoints.

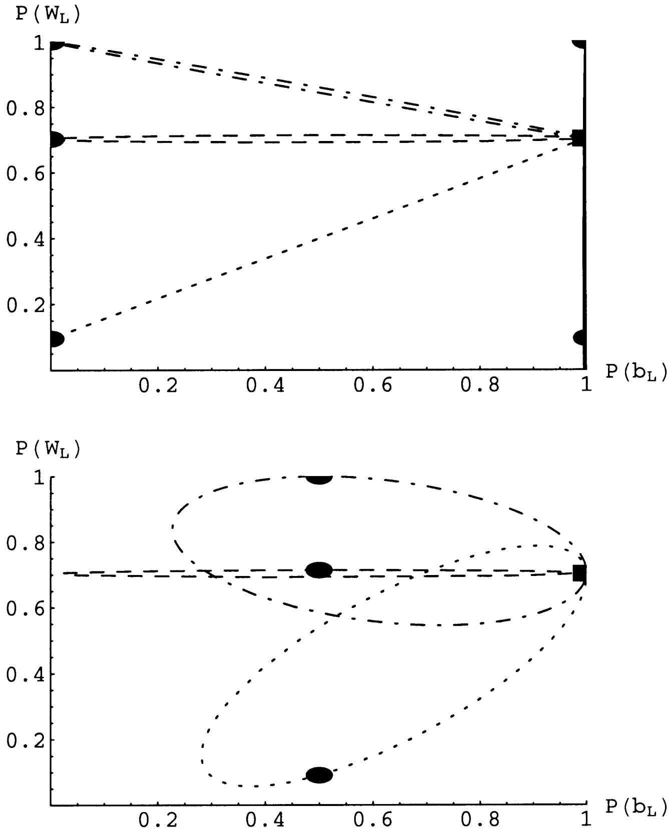

Fig. 2. For the case of a single additional coupling (g_i), plots of the probability, $P(W_L)$, that the emitted W^+ is "Longitudinally" polarized versus the probability, $P(b_L)$, that the emitted b-quark has "Left-handed" helicity. The **upper plot** is for additional chiral couplings: a dark rectangle denotes the value for the pure $V-A$ coupling of the standard model. The long-dashed (horizontal) oval is for an additional $V+A$ coupling. A dark ellipse denotes the end point where the coupling is pure $V+A$, and similarly for the other ovals. The dashed (zero area) oval is for an additional $f_M - f_E$ coupling. The dashed-dot oval is for an addition $S-P$ coupling. The solid (zero-area) vertical ovals with $P(b_L) = 1$ which end above/below the $V-A$ point are for an additional $S+P$ / f_M+f_E coupling. The upper(lower) portions of the ovals are for $\Lambda_i > 0 (< 0)$, except for the solid curves $f_M + f_E$ and $S+P$ which cover the full $P(W_L)$ range for small Λ_i values, see the $P(W_L)$ versus Λ_i plots in Fig. 3. The **lower plot** is for additional non- chiral coupling V, S, f_M couplings. The long-dashed (horizontal) oval is for an additional $V(A)$ coupling. The dashed oval is for an additional $f_M(f_E)$ coupling. The dashed-dot oval is for an addition $S(P)$ coupling. $\Lambda_i > 0$ corresponds to the tops of the ovals from the $V-A$ solid rectangle to the pure g_i endpoints. To the eye, the omitted respective curves for A, P, f_E almost overlap the ones for V, S, f_M. For A, the endpoint is slightly below (that for V) and on the bottom arc of its oval

The lower plot in Fig. 2 is for the case of a single additional non-chiral coupling V, S, f_M (A, P, f_E). The cor-

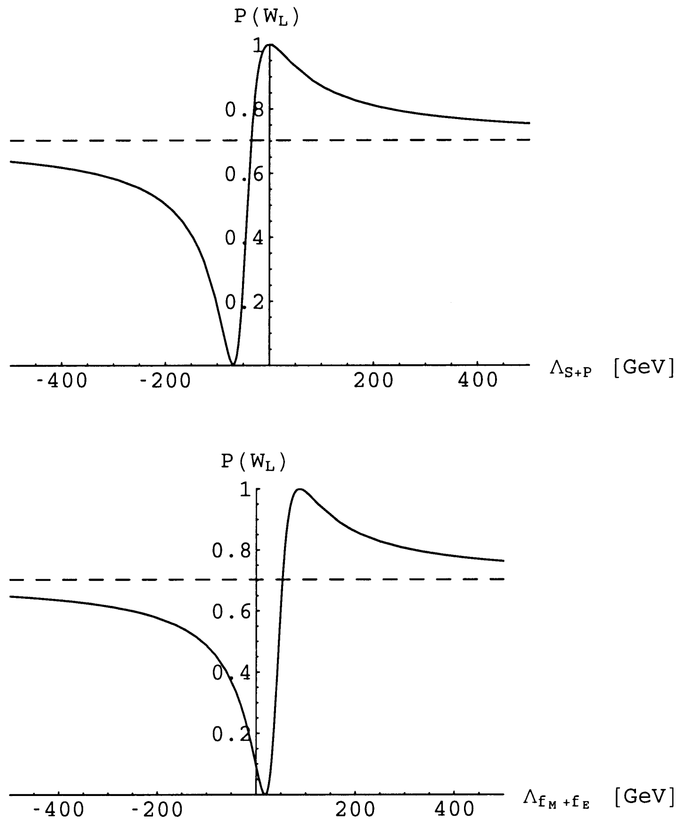

Fig. 3. The **upper(lower) plot** displays the $P(W_L)$ value versus the effective-mass scale Λ for an additional $S+P$ ($f_M + f_E$) coupling. The ambiguous- moduli point for this coupling occurs at $\Lambda_{S+P} \sim -34.5GeV$ ($\Lambda_{f_M+f_E} \sim 52.9GeV$) where the solid curve crosses over the dashed horizontal line which shows the standard V-A value

responding ovals in the two non-chiral plots are almost identical in shape. The g_V (g_A) endpoints lie on the upper(lower) parts of their ovals. In this paper, we omit the A, P, f_E curves corresponding to the ones provided for V, S, f_M because by Lorentz invariance the corresponding ovals, etc., are almost identical, see figure captions.

3 Moduli parameters and phase-type ambiguities

Versus predictions based on the SM, two phase-type ambiguities arise by consideration of the effects of a single additional "chiral" coupling g_i on the three moduli parameters $\sigma = P(W_L) - P(W_T)$, $\xi = P(b_L) - P(b_R)$, and $\zeta = \frac{1}{\Gamma}(\Gamma_L^{b_L - b_R} - \Gamma_T^{b_L - b_R})$. The partial width Γ for $t \to W^+ b$ is the remaining and very important moduli parameter for testing for additional Lorentz structures. Since Γ sets the overall scale, it cannot be well measured by spin-correlation techniques, which better measure the ratios of moduli and relative phases, so we consider Γ separately; see also [14].

For an additional $S + P$ coupling with $\Lambda_{S+P} \sim -34.5$ GeV the values of (σ, ξ, ζ) and also of the partial width Γ are about the same as the SM prediction, see Table 2. This is the first ambiguity. The dependence of the $P(W_L)$ value versus the effective-mass scale Λ_{S+P} is shown in the upper plot in Fig. 3. Table 1 shows that this ambiguity will also occur if the sign of the $A_X(0, -\frac{1}{2})$ amplitude for $g_L + g_X$ is taken to be opposite to that of the SM's amplitude. Recall that an additional $S \pm P$ only effects the longitudinal $W^\pm$ amplitudes and not the transverse $\lambda_W = \mp 1$ ones. By requiring that

$$\frac{A_X(0, -\frac{1}{2})}{A_X(-1, -\frac{1}{2})} = - \frac{A_L(0, -\frac{1}{2})}{A_L(-1, -\frac{1}{2})} \tag{8}$$

for $X = S + P$, we obtain a simple formula

$$\begin{aligned} \Lambda_{S+P} &= - \left(\frac{g_{S+P}}{g_L} \right) \frac{m_t \, q_W}{2(E_W + q_W)} \\ &\sim - \left(\frac{g_{S+P}}{g_L} \right) \frac{m_t}{4} \left(1 - \left(\frac{m_W}{m_t} \right)^2 \right) . \end{aligned} \tag{9}$$

It is important to regard these ambiguities from (i) the signs in their b_L amplitudes versus those for the SM and from (ii) the tensorial character and Λ value of the associated Lorentz structure.

For an additional $f_M + f_E$ coupling with $\Lambda_{f_M+f_E} \sim 53GeV$ the values of (σ, ξ, ζ) are also about the same as the SM prediction, see Table 2. This is the second ambiguity. In this case, the partial width Γ is about half that of the SM due to destructive interference. The dependence of the $P(W_L)$ value versus the effective-mass scale $\Lambda_{f_M+f_E}$ is shown in the lower plot of Fig. 3. Table 1 shows that this ambiguity will also occur if the sign of the $A_X(-1, -\frac{1}{2})$ amplitude for $g_L + g_X$ is taken to be opposite to that of the SM's amplitude. Again, from (8) for $X = f_M + f_E$, we obtain

$$\begin{aligned} \Lambda_{f_M+f_E} &= \left(\frac{g_{f_M+f_E}}{g_L} \right) \frac{m_t E_W}{2(E_W + q_W)} \\ &\sim \left(\frac{g_{f_M+f_E}}{g_L} \right) \frac{m_t}{4} \left(1 + \left(\frac{m_W}{m_t} \right)^2 \right) \end{aligned} \tag{10}$$

since $\frac{m_b}{m_t} \frac{\sqrt{E_b - q_W}}{\sqrt{E_b + q_W}} \sim 10^{-3}$.

Besides the $f_M + f_E$ construction of this second phase-type ambiguity, it should be kept in mind that some other mechanism might produce the relative sign change shown in Table 1, but without also changing the absolute value of the b_L amplitudes. In this case the measurement of the partial width Γ would not resolve the phase ambiguity.

These phase-type ambiguities are, of course, not the same dynamical issue as finding a combination of $f_M + f_E$ and $S+P$ couplings which give the identical b_L amplitudes as for a pure $V - A$ coupling. By the expressions in Appendix A, this is possible if $\Lambda_{S+P} = -\Lambda_{f_M+f_E} = \frac{m_t}{2}(1 - (\frac{m_b}{m_t})^2) = 87GeV$ and a negligible (for b_L amplitudes) $\Lambda_{S-P} = -\Lambda_{f_M-f_E} = -\frac{(m_t)^2}{2m_b}(1 - (\frac{m_b}{m_t})^2) = -3,401GeV$. The b_R amplitudes are identical to those for a pure $V - A$

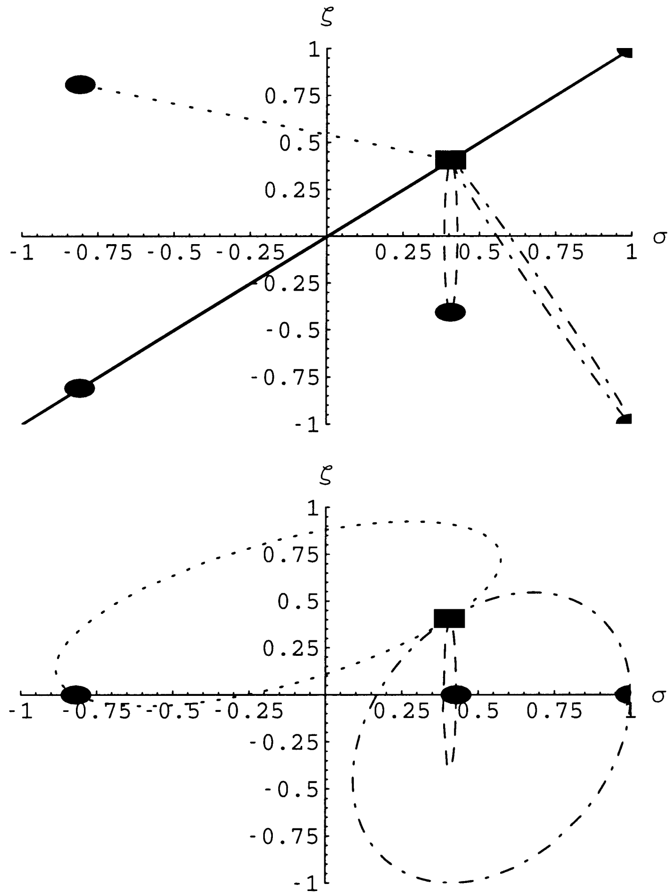

Fig. 4. For the case of a single additional coupling (g_i), plots of the moduli parameters ζ versus σ. The ovals are labeled as in Fig. 2. $\Lambda_i > 0$ corresponds to the right-sides of the ovals from the $V-A$ rectangle to the pure g_i endpoints. In the **upper plot** for additional chiral couplings, the $S+P$ (f_M+f_E) endpoint is in the first(third) quadrant. The **lower plot** is for additional V, S, f_M couplings. To the eye, the omitted respective curves for A, P, f_E almost overlap. The A endpoint is slightly to the left, on the origin side of the oval

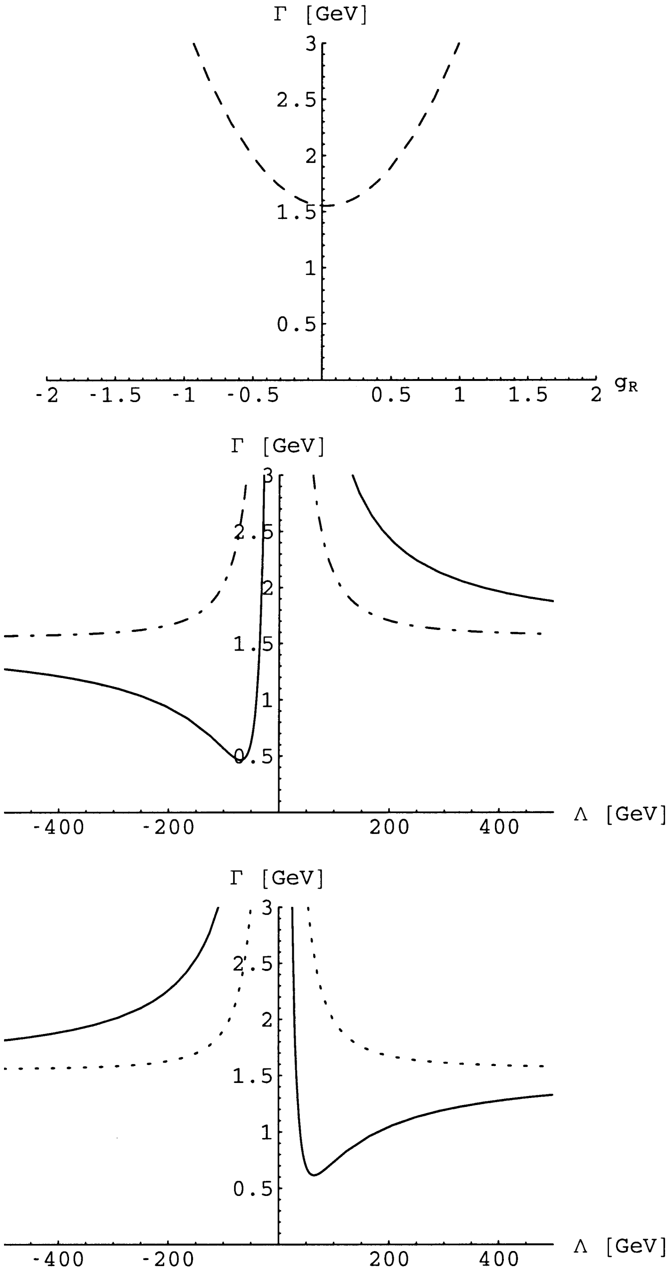

Fig. 5. Plots of the partial width for $t \to W^+b$ versus strengths of an additional chiral coupling: upper-figure is for an additional $V+A$ coupling; middle-figure's solid (dashed-dot) curve is for $S+P$ ($S-P$); and lower-figure's solid (dashed-dot) curve is for f_M+f_E (f_M-f_E)

coupling because of (same order of magnitude) contributions from all of $S \pm P, f_M \pm f_E$. Without the $\Lambda \sim -3,401GeV$ scale couplings, the b_R amplitudes are $A_X(0,\frac{1}{2}) = 6.37, A_X(1,\frac{1}{2}) = -1.51$ for $X = (S+P) + (f_M+f_E)$ to be compared with the different $V-A$ entries in the top line of Table 1. Alternatively with non-chiral couplings, the standard model's fundamental V coupling is equivalent to $\Lambda_S = -\Lambda_{f_M} = (m_t+m_b)/2$ and the fundamental $-A$ coupling to $\Lambda_P = -\Lambda_{f_E} = (m_t-m_b)/2$.

From consideration of Table 1, a third (phase) ambiguity can be constructed by making an arbitrary sign-flip in the b_L amplitudes, so $A_X(\lambda_W,\lambda_b = -\frac{1}{2}) = -A_{V-A}(\lambda_W, \lambda_b = -\frac{1}{2})$, with no corresponding sign changes in the b_R amplitudes. Resolution of this ambiguity will require b-polarimetry.

In Fig. 4 are plotted the moduli parameter ζ versus σ for the case of a single additional coupling g_i. The figures are for the case of an additional chiral (non-chiral) coupling.

From the perspective of possible additional Lorentz structures, measurement of the partial width Γ is an important constraint. In particular, this provides a strong constraint on possible $V+A$ couplings, see top part of Fig. 5, in contrast to measurement of $P(W_L)$ which does not, recall Fig. 2. The remaining parts of Fig. 5 are for $S \pm P$ ($f_M \pm f_E$). Likewise, as shown in the top part of Fig. 6, Γ provides a useful constraint for the possibility of additional V and A couplings which are appealing from the perspective of additional gauge-theoretic structures.

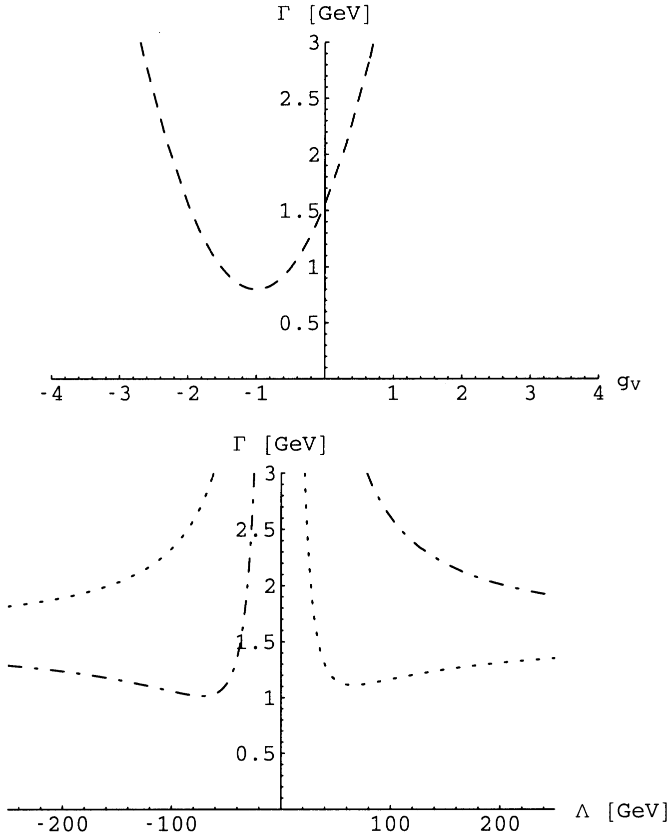

Fig. 6. Plots of the partial width for $t \to W^+ b$ versus strengths of an additional non-chiral coupling V, S, f_M: upper-figure is for an additional V coupling; and lower- figure's dashed-dot (dotted) curve is for S (f_M). The omitted plot for A is almost the mirror image about the Γ axis of V's, so $\Gamma(g_A) \approx \Gamma(-g_V)$. Those for P, f_E are respectively about the same as for S, f_M

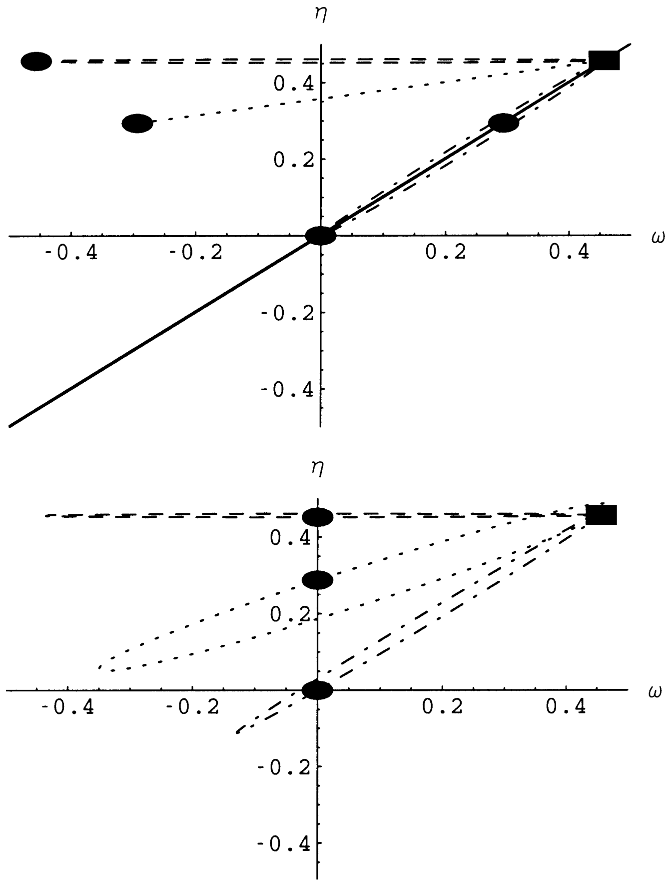

Fig. 7. Plots of the two W-polarimetry interference parameters, η, ω for the case of a single additional coupling (g_i). The ovals are labeled as in Fig. 2. $\Lambda_i > 0$ correspond to the lower parts of the ovals from the $V-A$ rectangle to the pure g_i endpoints, except for the omitted P curve where it is the upper part. The **upper plot** is for additional chiral couplings and the first two phase-type ambiguities correspond to a "pseudo-image of the SM rectangle" at $(-0.46, -0.46)$. The $S \pm P$ end points are at the origin. On the solid line (zero area) ovals, the $f_M + f_E$ end point is in the first quadrant, and both the $f_M + f_E$ and $S + P$ ovals extend through the third quadrant with respectively $\Lambda_i > 0, < 0$. The $f_M + f_E$ and $S + P$ ovals each cover the entire diagonal. The **lower plot** is for additional V, S, f_M (A, P, f_E) couplings. On the vertical axis, the $V(A)$ end point is at the bottom(top) of its horizontal oval. Similarly, near the origin the $S(P)$ end point is at the bottom(top) of its oval

Here also, the lower part of this figure is for an additional S, f_M (P, f_E) coupling.

4 Phase parameters and interference measurements

In Fig. 7 are plotted the W-polarimetry interference parameters η versus ω for the case of a single additional coupling g_i. The figures are for the case of an additional chiral (non-chiral) coupling. Quite dramatically in the upper plot, the $S{+}P$ and $f_M{+}f_E$ ambiguities both correspond to a "pseudo-image of the SM rectangle". This image is in the third quadrant on the diagonal at $(\eta, \omega) = (-0.46, -0.46)$. As shown in the bottom part of Table 2, measurement of the signs of either η or ω will resolve both the $S + P$ and the $f_M + f_E$ phase-type ambiguities. In the SM, these parameters are sizable and are equal if the b_R amplitudes are omitted, see (2,3).

Determination of the α and γ interference phases, as well as resolution of the third ambiguity, will require direct empirical information about the b_R amplitudes. In Fig. 8 are plotted the b-polarimetry interference parameter ϵ_+, versus η_L, for the case of a single additional coupling g_i. Similarly, in Fig. 9 are plotted the b-polarimetry interference parameter κ_0, versus η_L. The upper (lower) figures are respectively for the case of an additional non-chiral (chiral) coupling. Here in general, the non-chiral couplings produce larger deviations versus the SM's prediction, i.e. the dark rectangle. In particular, additional $S + P$ and $f_M + f_E$ couplings have negligible effects on ϵ_+ and κ_0. Not shown in these figures for (ϵ_+, η_L) and (κ_0, η_L) is the unitarity limit, which is a circle of radius $\frac{1}{2}$ centered on the origin.

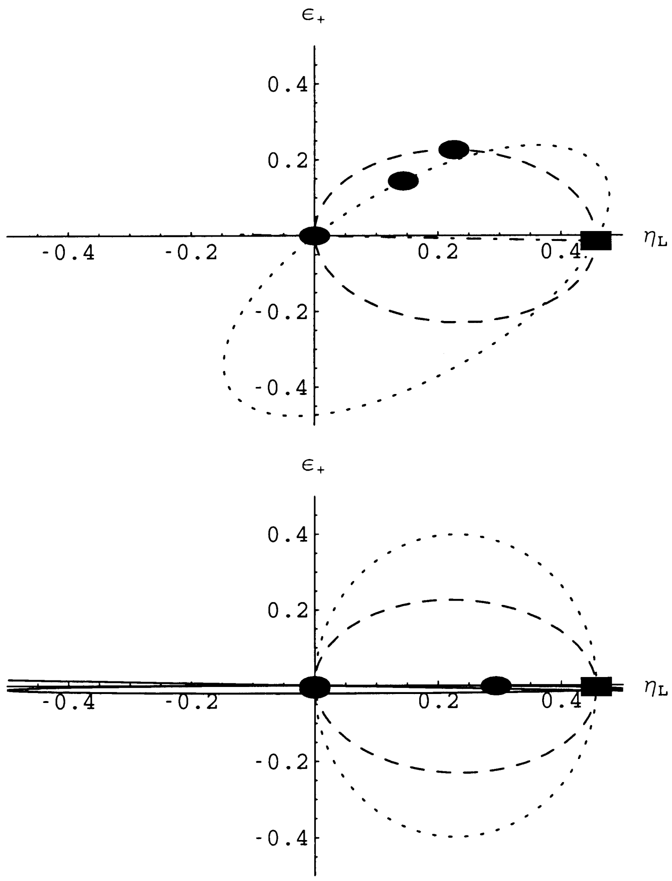

Fig. 8. Plots of the b-polarimetry interference parameter ϵ_+ versus η_L for the case of a single additional coupling (g_i). The **upper plot** is for additional V, S, f_M couplings. $\Lambda_i > 0$ corresponds to the upper part of the long-dashed V oval from the $V-A$ rectangle, the lower part of the dotted f_M, and one of the positive η_L parts of the dashed- dot S. The latter, zero-area S oval extends to $\eta_L \sim -1.2$. The omitted A, P, f_E plot is almost the mirror image about the η_L axis, in it $\Lambda_i > 0$ corresponds to the upper parts of the long-dashed A and dotted f_E ovals from the $V-A$ rectangle, and one of the positive η_L parts of the dashed-dot P. The **lower plot** is for a single additional chiral coupling. Only the $f_M + f_E$ endpoint is not near the origin. The ϵ_+ values are non- negligible for only two couplings: $\Lambda_i > 0$ corresponds to the upper part of the long-dashed $V+A$ oval from the $V-A$ rectangle, the lower part of the dotted $f_M - f_E$ oval. For the other couplings, their $\eta_L = \frac{1}{2}(\eta + \omega)$ dependence is shown in Fig. 7

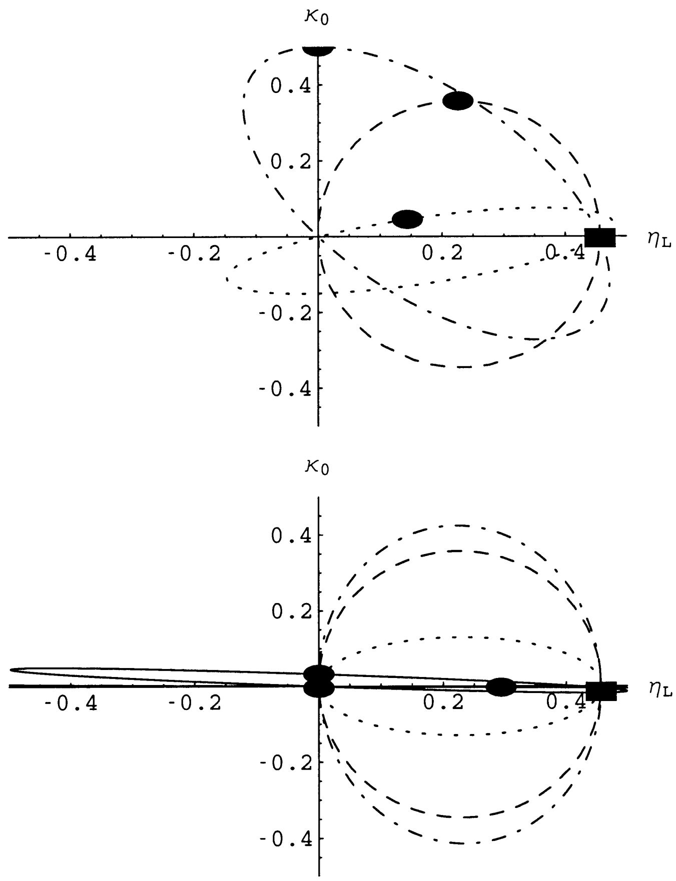

Fig. 9. Plots of the b-polarimetry interference parameter κ_0 versus η_L for the case of a single additional (g_i). The **upper plot** is for additional V, S, f_M couplings. $\Lambda_i > 0$ corresponds to the upper part of the long-dashed V and the dashed-dot S ovals from the $V-A$ rectangle, and corresponds to the lower part of the dotted f_M. The omitted A, P, f_E plot is almost the mirror image about the η_L axis. In it, $\Lambda_i > 0$ corresponds to the upper parts of the long-dashed A and dotted f_E ovals from the $V-A$ rectangle, and corresponds to the lower part part of the dashed-dot P. The **lower plot** is for a single additional chiral coupling. Only the $f_M + f_E$ endpoint is not near the origin. The κ_0 values are non-negligible for three couplings: $\Lambda_i > 0$ corresponds to the upper part of the long-dashed $V+A$ and dashed-dot $S-P$ ovals from the $V-A$ rectangle, and corresponds to the lower part of the dotted $f_M - f_E$ oval

5 Ambiguities among other Lorentz structures

From the plots for the various helicity parameters, it is evident that there also are ambiguities within certain subsets of the couplings if an additional Lorentz structure were to occur in the form of a single additional g_i. The occurrence of an additional Lorentz structure would also raise the issue of how to determine the sign (or phase) of its Λ_i.

The following equivalence classes among additional Lorentz structures (versus subsets of possible experimental tests) is another consequence of the underlying Lorentz invariance of (6, 7), etc. Second, with only W-polarimetry, the effects of the non-zero m_b mass ($m_b = 4.5GeV$) are negligible for (i) additional gauge couplings $V, A, V+A$ and for (ii) additional chiral couplings. However, there is a sizable m_b dependence in some chiral couplings in the (ϵ_+, η_L) and (κ_0, η_L) plots. In general for additional S, P, f_M, f_E couplings, the dependence on m_b is sizable and is likely to be a serious systematic effect in data analysis.

5.1 Additional $V+A, V$, or A couplings

From the gauge theory viewpoint, it is important to search for additional vector and axial vector couplings. The SM's $P(W_L)$ and η values are only slightly affected by them. But the values for $P(b_L)$, ζ, ω, ϵ_+, and κ_0 are significantly different from those of the SM. However, inspection of the figures shows that in many of the plots the ovals for $V+A, V, A$ are approximately degenerate. Nevertheless, from the different locations of their endpoints in Figs. (8-9), the $\epsilon_+, \eta_L, \kappa_0$ parameters could be useful in resolving them. So b-polarimetry or Γ would generally be useful to resolve these additional couplings and to determine the sign of the associated Λ_i .

5.2 Additional $S-P, S$, or P couplings

For S, P, versus $S-P$ there are differences in some of the plots but sufficient resolution and control of possible m_b effects would be needed. In particular, the narrow $S-P$ oval and the degenerate fat S, P ovals lie approximately in the same $P(W_L), P(b_L)$ regions and also in the same ζ, σ regions. The sign of Λ_i is the same for the S and P ovals. If $\eta, \omega < 0$, it would exclude $S-P$ and would determine the respective sign of Λ_i. The κ_0, η_L plot is useful for distinguishing S versus P and for the sign of Λ_i. If $S-P$ were resolved, then κ_0 would give the sign of Λ_i. Γ is not useful for separating S versus P, but Γ is different for $S-P$.

5.3 Additional $f_M + f_E$ or $S+P$ couplings

$f_M + f_E$ and $S+P$ can be distinguished from either the $P(W_L), P(b_L)$ or ζ, σ plots. Once separated, Γ could provide information on the sign of Λ_i. If $\eta, \omega < 0$, it would determine the respective sign of Λ_i. $\epsilon_+ \simeq \kappa_0 \simeq 0$ for these couplings.

5.4 Additional $f_M - f_E$, f_M, or f_E couplings

With sufficient resolution and control of m_b effects, $f_M - f_E$ could be separated versus f_M, f_E by $P(W_L), P(b_L)$; by the ζ, σ plot; and/or by Γ. The ϵ_+,η_L plot would be useful for separating f_M from f_E and in determining the sign of Λ_i. It would also determine the sign for $f_M - f_E$.

Acknowledgements. For computer services, we thank Mark Stephens. One of us(CAN) thanks the Fermilab Theory Group for a visit. This work was partially supported by U.S. Department of Energy Contract No. DE-FG 02-96ER40291.

Appendices

A Lorentz equivalence theorems

In the case of non-chiral couplings and with the signs and normalizations of (6,7), the tensorial f_M coupling can be absorbed by using

$$g'_V = g_V - (m_t + m_b)\frac{f_M}{2\Lambda_M}, \quad \frac{g'_S}{2\Lambda'_S} = \frac{g_S}{2\Lambda_S} + \frac{f_M}{2\Lambda_M}, \quad (11)$$

or alternatively, the scalar S coupling can be absorbed

$$g'_V = g_V + (m_t + m_b)\frac{g_S}{2\Lambda_S}, \quad \frac{f'_M}{2\Lambda'_M} = \frac{f_M}{2\Lambda_M} + \frac{g_S}{2\Lambda_S}. \quad (12)$$

Similarly, f_E can be absorbed by

$$g'_A = g_A + (m_t - m_b)\frac{f_E}{2\Lambda_E}, \quad \frac{g'_P}{2\Lambda'_P} = \frac{g_P}{2\Lambda_P} + \frac{f_E}{2\Lambda_E}, \quad (13)$$

or alternatively P by

$$g'_A = g_A - (m_t - m_b)\frac{g_P}{2\Lambda_P}, \quad \frac{f'_E}{2\Lambda'_E} = \frac{f_E}{2\Lambda_E} + \frac{g_P}{2\Lambda_P}. \quad (14)$$

The g_{T^+} is absorbed by $g_V \to g'_V = g_V - (m_t - m_b)\frac{g_{T^+}}{2\Lambda_{T^+}}$ and $g_{T_5^+}$ by $g_A \to g'_A = g_A + (m_t + m_b)\frac{g_{T_5^+}}{2\Lambda_{T_5^+}}$.

In the case of the chiral combinations, the tensorial $g_\pm \equiv f_M \pm f_E$ are absorbed by using

$$\begin{aligned} g'_L &= g_L - m_t\tfrac{g_+}{2\Lambda_+} - m_b\tfrac{g_-}{2\Lambda_-}, \quad \tfrac{g'_{S+P}}{2\Lambda'_{S+P}} = \tfrac{g_{S+P}}{2\Lambda_{S+P}} + \tfrac{g_+}{2\Lambda_+}, \\ g'_R &= g_R - m_t\tfrac{g_-}{2\Lambda_-} - m_b\tfrac{g_+}{2\Lambda_+}, \quad \tfrac{g'_{S-P}}{2\Lambda'_{S-P}} = \tfrac{g_{S-P}}{2\Lambda_{S-P}} + \tfrac{g_-}{2\Lambda_-}, \end{aligned} \quad (15)$$

or alternatively $S \pm P$ by

$$\begin{aligned} g'_L &= g_L + m_t\tfrac{g_{S+P}}{2\Lambda_{S+P}} + m_b\tfrac{g_{S-P}}{2\Lambda_{S-P}}, \quad \tfrac{g'_+}{2\Lambda'_+} = \tfrac{g_+}{2\Lambda_+} + \tfrac{g_{S+P}}{2\Lambda_{S+P}}, \\ g'_R &= g_R + m_t\tfrac{g_{S-P}}{2\Lambda_{S-P}} + m_b\tfrac{g_{S+P}}{2\Lambda_{S+P}}, \quad \tfrac{g'_-}{2\Lambda'_-} = \tfrac{g_-}{2\Lambda_-} + \tfrac{g_{S-P}}{2\Lambda_{S-P}}. \end{aligned} \quad (16)$$

The $\tilde{g}_\pm = g_{T^+} \pm g_{T_5^+}$ are absorbed by $g_L \to g'_L = g_L - m_t\frac{\tilde{g}_+}{2\tilde{\Lambda}_+} + m_b\frac{\tilde{g}_-}{2\tilde{\Lambda}_-}$ and $g_R \to g'_R = g_R - m_t\frac{\tilde{g}_-}{2\tilde{\Lambda}_-} + m_b\frac{\tilde{g}_+}{2\tilde{\Lambda}_+}$

B Formulas for α, β, γ phases from helicity parameters

Equations (2,3) define the W^+ longitudinal/transverse interference parameters $\eta_{L,R}$ associated with the $\beta_{L,R}$ phases. Similarly, from Fig. 1 the parameters associated with the $\alpha_{0,1}$ and $\gamma_\pm$ phases are

$$\begin{aligned} \kappa_0 &= \tfrac{1}{2}(\lambda + \kappa) \equiv \tfrac{1}{\Gamma}|A(0,-\tfrac{1}{2})||A(0,\tfrac{1}{2})|\cos\alpha_0 \\ \kappa_1 &= \tfrac{1}{2}(\lambda - \kappa) \equiv \tfrac{1}{\Gamma}|A(-1,-\tfrac{1}{2})||A(1,\tfrac{1}{2})|\cos\alpha_1 \\ \epsilon_+ &= \tfrac{1}{2}(\delta + \epsilon) \equiv \tfrac{1}{\Gamma}|A(1,\tfrac{1}{2})||A(0,-\tfrac{1}{2})|\cos\gamma_+ \\ \epsilon_- &= \tfrac{1}{2}(\delta - \epsilon) \equiv \tfrac{1}{\Gamma}|A(-1,-\tfrac{1}{2})||A(0,\tfrac{1}{2})|\cos\gamma_- \end{aligned} \quad (17)$$

The corresponding primed parameters are defined by replacing the cosine by sine.

The inverse formulas for $\cos\beta_{L,R}$, $\sin\beta_{L,R}$ from $\eta_{L,R}$ and $\eta'_{L,R}$ are given by (56-59) in [5]. For extracting the

$\alpha_{0,1}$ and $\gamma_\pm$ phases,

$$\begin{aligned}
\cos\alpha_0 &= \frac{4\kappa_0}{\sqrt{(1+\sigma)^2-(\xi+\zeta)^2}} \\
\cos\alpha_1 &= \frac{4\kappa_1}{\sqrt{(1-\sigma)^2-(\xi-\zeta)^2}} \\
\cos\gamma_+ &= \frac{4\epsilon_+}{\sqrt{(1+\zeta)^2-(\sigma+\xi)^2}} \\
\cos\gamma_- &= \frac{4\epsilon_-}{\sqrt{(1-\zeta)^2-(\sigma-\xi)^2}}
\end{aligned} \qquad (18)$$

and the sine's of the respective angles are obtained by using the primed helicity parameter in the respective numerator.

References

1. F. Abe, et al. (CDF collaboration), Phys. Rev. Lett. **74**, 2626 (1995); S. Abachi, et al. (D0 collaboration), Phys. Rev. Lett. **74**, 2632 (1995).
2. ATLAS Technical Proposal, CERN/LHCC/94-43, LHCC/P2 (1994); CMS Technical Design Report, CERN-LHCC- 97-32; CMS-TDR-3 (1997).
3. Reports on work for Next Linear Colliders by B. Wiik (DESY), H. Sugawara (KEK), B. Richter (SLAC) at ICHEP98, Vancouver, Canada (to be published).
4. G. 't Hooft, THU-94/15; S. Weinberg, in "Unification of Elementary Forces and Gauge Theories", eds. D.B. Cline, F.E. Mills (harwood, London, 1978).
5. C.A. Nelson, B.T. Kress, M. Lopes, T.P. McCauley, Phys. Rev. D **56**, 5928 (1997); D **57**, 5923 (1998). The relations between the chiral and non-chiral couplings are $g_{chiral} = g_1 \pm g_2$; e.g. $g_L = g_V - g_A, g_R = g_V + g_A, g_{S\pm P} = g_S \pm g_P, g_\pm = f_M \pm f_E$. This has produced a factor of 2 change in the horizontal axis in Fig. 6 versus the non-chiral plots and tables in hep-ph/9806373. Since in $g_L = 1$ units the numerical value of a specific Λ_i is determined by fixing its $g_i = 1$, the sign of Λ_i gives the relative sign of the $g_i/(2\Lambda_i)$ coupling versus g_L.
6. G.J. Gounaris, F.M. Renard, C. Verzegnassi, Phys. Rev. D **52**, 451 (1995); G.J. Gounaris, D.T. Papadamou, F.M. Renard, Z. Phys. C **76**, 333 (1997).
7. A. Bartl, E. Christova, W. Majerotto, Nucl. Phys. B **460**, 235 (1996); A. Bartl, E. Christova, T. Gajdosik, W. Majerotto, Phys. Rev. **D58**, 074007 (1998); hep-ph/9803426.
8. B. Lampe, Phys. Lett. B **415**, 63 (1997); B. Grzadkowski, Z. Hioki, M. Szafranski, hep-ph/9712357.
9. K. Whisnant, J.M. Yang, B.-L. Young, Z. Zhang, Phys. Rev. D **56**, 467 (1997); J.M. Yang, B.- L. Young, ibid.,D **56**, 5907 (1997); J.-J. Cao, et al., hep-ph/9804343.
10. F. Larios, E. Malkawi, C.-P. Yuan, Acta Phys. Polon. B **27**, 3741 (1996); hep-ph/9704288; H.-J. He, Y.-P. Kuang, C.-P. Yuan, hep-ph/9704276.
11. G. Mahlon, S. Parke, Phys. Rev. **D55**, 7249 (1997); Phys. Lett. **B411**, 173 (1997); G. Mahlon hep-ph/9810485, hep-ph/9811281.
12. Y.Zeng-Hui, H. Pietschmann, M. Wen-Gan, H. Liang, J. Yi, hep-ph/9804331.
13. M. Jezabek, J.H. Kuhn, Phys. Lett. **B207**, 91 (1988); B **329**, 317 (1994); Nuc. Phys. B **314**, 1 (1989); B **320**, 20 (1989); C.S. Li, R. Oakes, T.C. Yuan, Phys. Rev. D **43**, 3759 (1991); T. Mehen, Phys. Lett. B **417**, 353 (1998); A. Czarnecki, K. Melnikov, hep- ph/9806244; B. Lampe, hep-ph/9810207.
14. A.S. Belyaev, E.E. Boos, L.V. Dudkov, hep-ph/9806332; A.P. Heinson, A.S. Belyaev, E.E. Boos, hep-ph/9612424; M.C. Smith, S.S. Willenbrock, Phys. Rev. **D54**, 6696 (1996); T.Stelzer, Z. Sullivan, S. Willenbrock, hep-ph/9807340; R. Pittau, Phys. Lett. **B386**, 397 (1996).